nature electronics

SUPPLEMENTARY INFORMATION

https://doi.org/10.1038/s41928-020-0385-0

In the format provided by the authors and unedited.

Skyrmion-based artificial synapses for neuromorphic computing

Kyung Mee Song[1], Jae-Seung Jeong[2], Biao Pan[3], Xichao Zhang[4], Jing Xia[4], Sunkyung Cha[1], Tae-Eon Park[1], Kwangsu Kim[1,5], Simone Finizio[6], Jörg Raabe[6], Joonyeon Chang[1,7], Yan Zhou[4], Weisheng Zhao[3], Wang Kang[3], Hyunsu Ju[2] and Seonghoon Woo[1,8] ✉

[1]Center for Spintronics, Korea Institute of Science and Technology, Seoul, Korea. [2]Center for Opto-Electronic Materials and Devices, Korea Institute of Science and Technology, Seoul, Korea. [3]Fert Beijing Institute, BDBC, and School of Microelectronics, Beihang University, Beijing, China. [4]School of Science and Engineering, The Chinese University of Hong Kong, Shenzhen, Guangdong, China. [5]Department of Physics, University of Ulsan, Ulsan, Korea. [6]Swiss Light Source, Paul Scherrer Institut, Villigen, Switzerland. [7]Department of Materials Science & Engineering, Yonsei University, Seoul, Korea. [8]IBM Thomas J. Watson Research Center, Yorktown Heights, NY, USA. ✉e-mail: shwoo@ibm.com

Supplementary Figures.

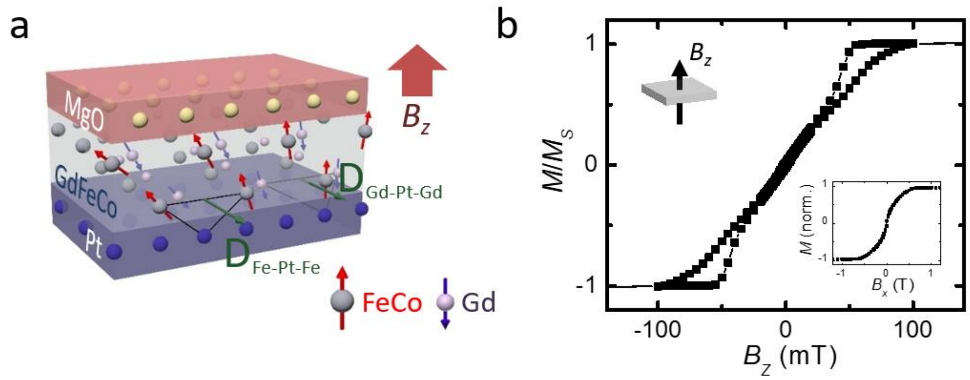

Supplementary Figure 1. Material, multilayer structure and magnetic properties. a, Schematic of Pt/GdFeCo/MgO ferrimagnetic multilayer structure, where magnetic moments of Gd and FeCo are antiferromagnetically coupled. Note that magnetic moments of Fe (Gd) are aligned parallel (anti-parallel) to an externally applied magnetic filed. Interface-induced Dzyaloshinskii-Moriya interaction (DMI) vectors favoring left-handed chirality are indicated with green arrows. In this asymmetric structure, underlying Pt induces strong interfacial DMI, inducing the formation of chiral magnetic skyrmions. **b,** Out-of-plane hysteresis loop of Pt/GdFeCo/MgO multilayer grown on a Si/SiO_x substrate measured by vibrating sample magnetometer (VSM). Inset shows the hysteresis loop corresponding to in-plane magnetic field application. VSM measurements yield the saturation magnetization and magnetic anisotropy field of M_s = 1.9 × 10^5 A m^{-1} and $\mu_0 H_k$ = 400 mT, respectively.

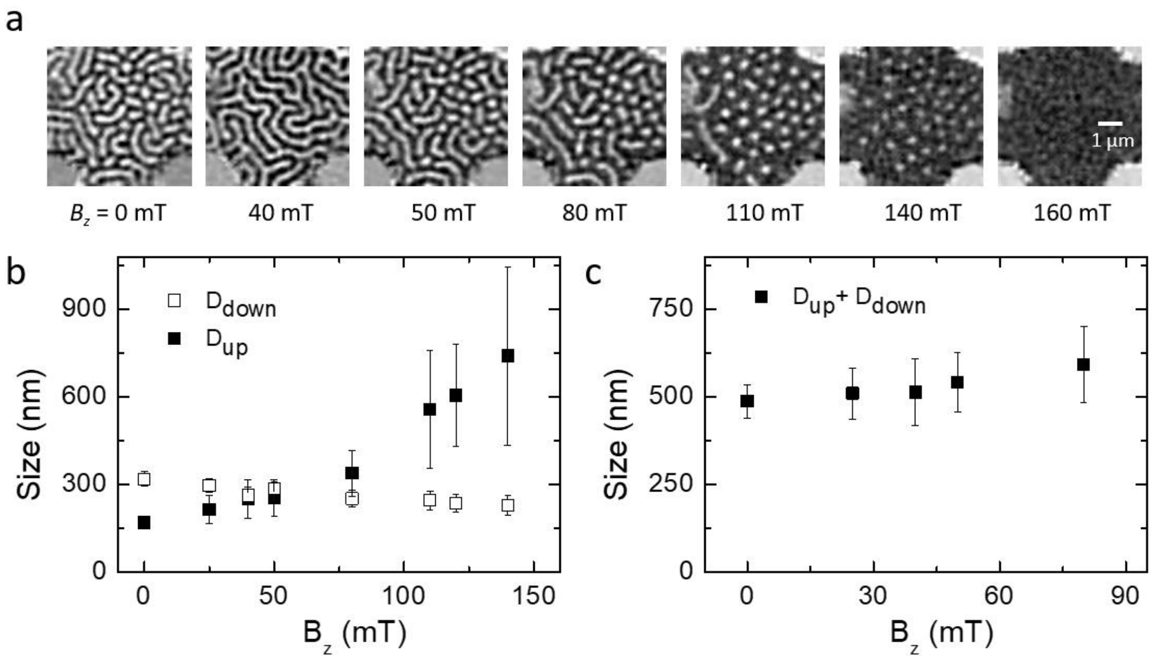

Supplementary Figure 2. Analytical calculation of the Dzyaloshinskii-Moriya interaction (DMI) constant using field-dependent magnetic domain configurations. **a**, Scanning transmission X-ray microscopy (STXM) images showing magnetic domain configuration at a given out-of-plane magnetic field, B_z, used for DMI constant calculation. **b**, Domain size (width) as a function of applied magnetic field for $B_z > 0$. **c**, Domain period ($D_{up}+D_{down}$) for relatively low field $B_z < 90$ mT, where the up-oriented domain width can be measured with reasonably small error. In this low field regime, the domain period is calculated to be ~530 nm. Considering that the domain width reflects the competition of energetic contributions including the demagnetizing energy, the domain wall (DW) energy, and DMI energy as studied in refs. [1–3], we can determine the DMI constant by calculating the DW surface energy from domain widths. Using the domain period at low field ($D_p = D_{up} + D_{down}$), we estimate the DW surface energy using the following equation: $\frac{\sigma_{DW}}{\mu_0 M_s^2 t} = \frac{D_p^2}{t^2} \sum_{odd\ n=1}^{\infty} \frac{1}{(\pi n)^3} \left[1 - \left(1+2\pi nt/D_p\right)\exp\left(-2\pi nt/D_p\right)\right]$. Using material parameters measured from the VSM measurements and the relation between domain wall surface energy and DMI constant, where $\sigma_{\mathrm{DW}} = 4\sqrt{AK_{\mathrm{u,eff}}} - \pi|D|$ with A the exchange stiffness, $K_{\mathrm{u,eff}}$ the effective uniaxial anisotropy constant, and D the DMI constant, our analysis yields the DMI constants of $|D|$ = 0.83 mJ m^{-2}. This DMI constant is in good agreement with the DMI constant measured in the same material system used for our previous study[4].

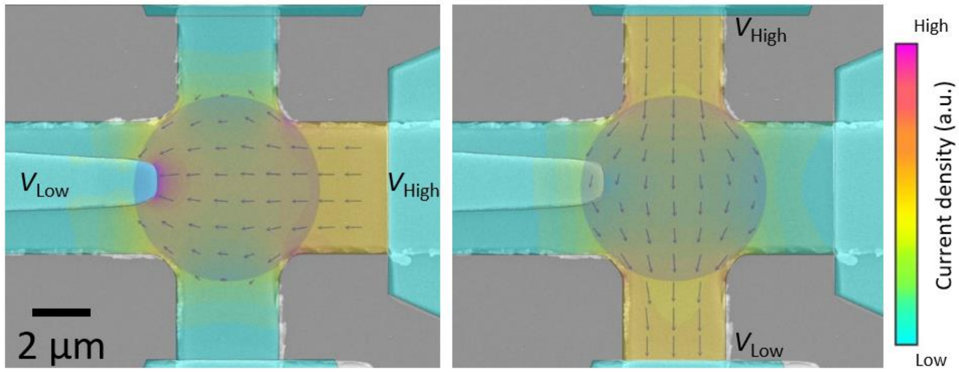

Supplementary Figure 3. Current density distribution simulation. Simulated distribution of current-denisty upon the application of voltage difference (V_{High} = 1 V and V_{Low} = 0 V) along the horizontal (left figure) and vertical (right figure) direction of Hall-cross geometry. The simulation was conducted using the Finite Element Method Magnetics (FEMM 4.2) open source simulation package developed by Aladdin Enterprises. The actual scanning electron microscopy (SEM) micrograph image of the measured device was used for analysis. The color scale corresponds to the relative amplitude of current density, and the current flow direction (against electron flow) and magnitude are indicated by enclosed arrows. Simulation result indicats that the charge current flows in circular fashion when passing through Hall-cross region, as non-negligible shunting current emerges due to the open structure. Therefore, we have considered the effective device area to be the area where the normalized current density $|j_0|/|j_{max}| > 0.05$ (5% error range), and this allows us to approximate a circular effective synapse region, $A_{synapse} \approx 38.1\ \mu m^2$. We have considered this effective synapse area for calculating the number of skyrmions.

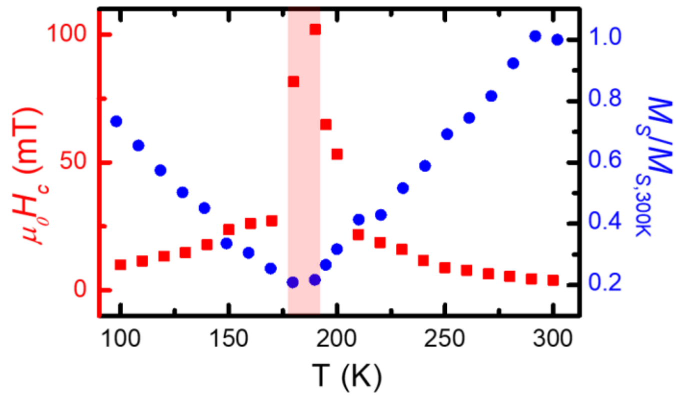

Supplementary Figure 4. Magnetization compensation temperature measurement. Temperature-dependent coercive magnetic field, $\mu_0 H_c$ (red, left axis), and normalized saturation magnetization, $M_S/M_{S,300K}$ (blue, right axis), in a Ta (3 nm)/Pt (3 nm)/GdFeCo (20 nm)/MgO (1 nm)/Ta (2 nm) unit structure grown on a thermally oxidized Si substrate measured by VSM. At $T < T_M$, where T_M is the magnetization compensation temeprature, the Gd moments dominate over the FeCo moments, resulting in the Gd mooments being aligned parallel to the external magnetic field, whereas the FeCo moments alings parallel to the field at $T > T_M$, As T approaches to T_M, the net magnetization converges to zero and the coercive magnetic field diverges as large Zeeman energy is required to siwtch the magnetization. This leads us to the conclusion that the magnetization compensation temperature of our structure is $T_M \approx 190$ K. Therefore, all experiments demonstrated in main text were performed at $T > T_M$, where FeCo (Gd) moments are aligned (anti-)parallel to the external magnetic field.

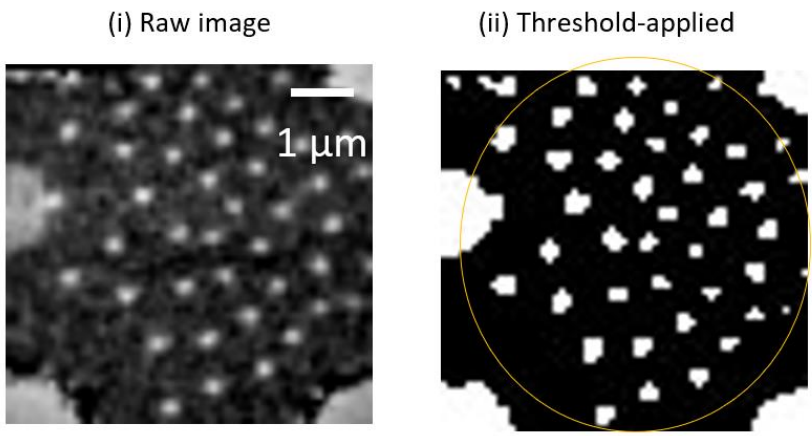

Supplementary Figure 5. Skyrmion number calculation using STXM images. Skymion number calculation was conducted using the embedded particle analyzer function within the ImageJ (ImageJ 1.52i) open source package. As shown above, we applied an image threshold considering the level of background noises, which then divides a raw image into a new image consists of two classes of pixels (black or white). The same condition of thresholding was applied to all images for consistency, and the threshold condition was acquired using first few images during potentiation (Fig. 2c in main text) where STXM image contrasts correspond to skyrmions are obvious. This image processing, combined with software-based skyrmion counting and visual confirmation, enabled us to correctly calculate the number of skyrmion at each resistivity state. Yellow solid line denotes the effective synapse area discussed in Supplementary Fig. S3.

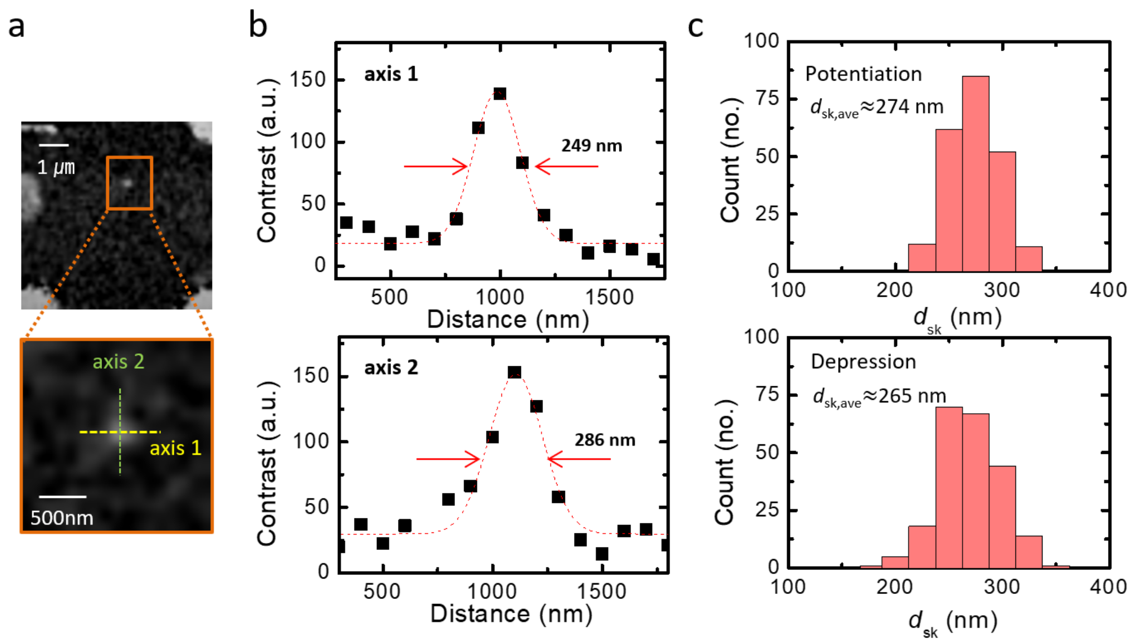

Supplementary Figure 6. Skyrmion size measurement and the diameter distribution during potentiation and depression. a, A representative scanning transmission X-ray microscopy (STXM) image where single skyrmion is located within the Hall-cross area, and the enlarged-STXM image. Image contrast profiles are extracted along two indicated lines (green and yellow). **b,** Results of image contrast line scans along yellow (upper panel) and green (lower panel) lines, respectively. The full-width half maximum (FWHM) values of gaussian fittings (plotted as dashed red lines) are used to calculate skyrmion diameters along each axis, and their root mean square value yields the effective skyrmion diameter. **c,** Extracted skyrmion size distribution during the potentiation and depression processes of skyrmion synapse, as shown in Fig. 2 in main text. Note that there exist skyrmion size distributions, mainly due to the imperfect nature of the material and inconsistent inter-skyrmion repulsions across synapse area influencing skyrmion radius variations.

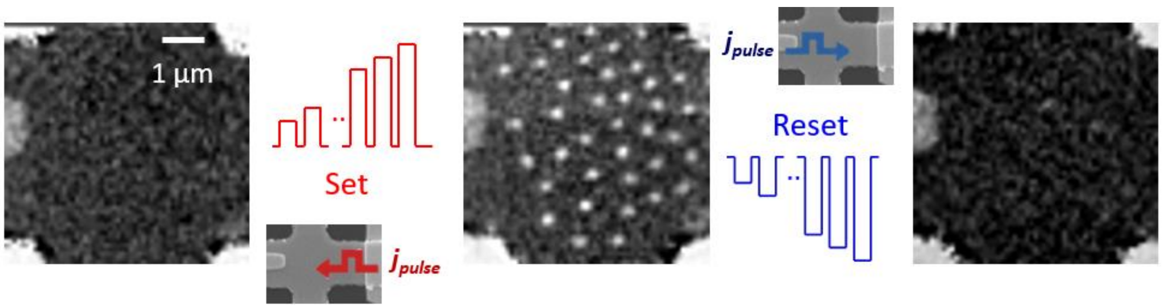

Supplementary Figure 7. ‘Set’ and ‘Reset’ operations of skyrmion synapse. After cycling potentiation-depression as shown in Fig. 2b in main text, we have examined ‘set’ and ‘reset’ operations of this skyrmion-based synapse by applying the burst of sequential pulses with the same pulse profile and acquiring scanning transmission X-ray microscopy (STXM) images. Pulse polarities are indicated above, where pulses are drawn as current flow, opposite to electron flow. For ‘set’ operation, we applied 25 successive pulses with systematically increasing current-density amplitudes of 1.69×10^{10} A m^{-2} < $|j_a|$ < 4.24×10^{10} A m^{-2} and pulse duration 100 ns. This operation results in the accumulation of 40 skyrmions and the resistivity of $\Delta\rho_{xy,\mathrm{f}} = -3.1 \times 10^2 \pm 4.1$ nΩ cm, in agreement with the final ‘set’ state acquired in Fig. 2 in main text within error range. Likely, for ‘reset’ operation, we reversed the polarity of gradually increasing pulses with the same condition and achieved completely saturated magnetization state as shown above. This demonstration of current-controlled fully ‘set’ and ‘reset’ states presents a key property required for artificial synaptic devices, which offers the programmable flexibility of skyrmion synapses together with multi-step potentiation/depression presented in main text.

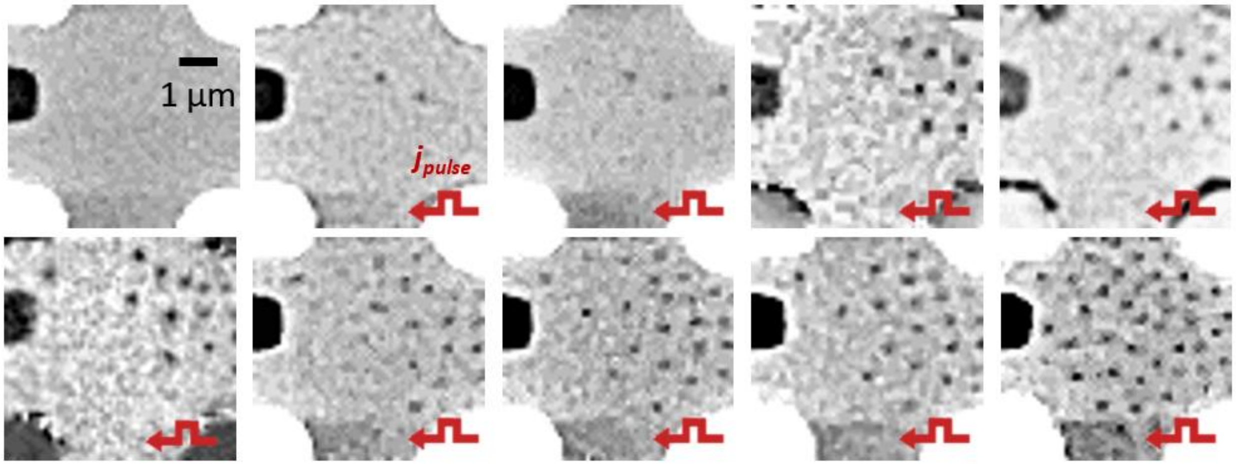

Supplementary Figure 8. ‘Potentiation’ operation of skyrmion synapse using magnetic skyrmions of core-up-m_z polarity. Sequential scanning transmission X-ray microscopy (STXM) images showing skyrmion populations after injecting unipolar current pulses along the device, with polarities as schematically indicated, during the potentiation process. As was used for the opposite polarity (core-up +m_z) skyrmions demonstrated in Figure 2 in a main text, current pulses with the gradually increasing current-density amplitudes of 1.69×10^{10} A m^{-2} < |j_a| < 4.24×10^{10} A m^{-2} and pulse duration of 100 ns were used at the external magnetic field of B_z = -140 mT.

Supplementary Tables.

	Skyrmion synapse	RRAM synapse
Energy Efficiency (TOPS/W)	1.21	1.85
Throughput (FPS)	87k	99k
Accuracy	93%	93%
Chip Area (μm2)	893k	598k
Chip Read Latency (ns)	11k	10k
Chip Read Dynamic Energy (pJ)	83k	54k
Chip Leakage Energy (pJ)	2.5k	2.2k

Supplementary Table 1. Circuit level performance of a simulated ANN chip for MNIST based on skyrmion and RRAM-based synaptic devices. The simulation is performed under 32 nm technology node with 5-bit synaptic weight.

	RRAM Synapse	Skyrmion Synapse
Parameter	Value	Value
Resistance-On	10kΩ	3kΩ
Resistance-Off	100kΩ	9kΩ
Read Voltage	0.1V	0.05V
Read Pulse Width	1ns	1ns
Access Voltage	1.4V	1V
Write Voltage	1.8V	30mV
Write Pulse Width	1ns	0.05ns
Cell Height	5F	14F
Cell Width	23F	44F
Cell bit	5 bits	5 bits
Number of States	32	32
Cell Type	1T1R	2T1R

Supplementary Table 2. Simulation parameters for RRAM and skyrmion-based artificial synapses.

Supplementary References.

S1. Woo, S. *et al.* Observation of room-temperature magnetic skyrmions and their current-driven dynamics in ultrathin metallic ferromagnets. *Nat. Mater.* 15, 501–506 (2016).

S2. Lemesh, I., Büttner, F. & Beach, G. S. D. Accurate model of the stripe domain phase of perpendicularly magnetized multilayers. *Phys. Rev. B* 95, 174423 (2017).

S3. Jaiswal, S. *et al.* Investigation of the Dzyaloshinskii-Moriya interaction and room temperature skyrmions in W/CoFeB/MgO thin films and microwires. *Appl. Phys. Lett.* 111, 022409 (2017).

S4. Woo, S. *et al.* Current-driven dynamics and inhibition of the skyrmion Hall effect of ferrimagnetic skyrmions in GdFeCo films. *Nat. Commun.* 9, 959 (2018).